

Article

Comparison between Single-Phase Flow Simulation and Multiphase Flow Simulation of Patient-Specific Total Cavopulmonary Connection Structures Assisted by a Rotationally Symmetric Blood Pump

Tong Chen ¹ , Xudong Liu ², Biao Si ³, Yong Feng ⁴, Huifeng Zhang ⁵, Bing Jia ^{5,*} and Shengzhang Wang ^{1,4,*} 

¹ Academy for Engineering and Technology, Fudan University, Shanghai 200433, China; 19110860027@fudan.edu.cn

² Shanghai Key Laboratory of Interventional Medical Devices and Equipment, Shanghai MicroPort Medical Group Co. Ltd., Shanghai 201203, China; xdliu@microport.com

³ Wallace H. Coulter School of Biomedical Engineering, Georgia Institute of Technology, Atlanta, GA 30332, USA; biao.si@bme.gatech.edu

⁴ Department of Aeronautics and Astronautics, Fudan University, Shanghai 200433, China; 18110290016@fudan.edu.cn

⁵ Department of Cardiothoracic Surgery, Children's Hospital of Fudan University, Shanghai 201102, China; zhanghuifeng@fudan.edu.cn

* Correspondence: jia_bing@fudan.edu.cn (B.J.); szwang@fudan.edu.cn (S.W.)



Citation: Chen, T.; Liu, X.; Si, B.; Feng, Y.; Zhang, H.; Jia, B.; Wang, S. Comparison between Single-Phase Flow Simulation and Multiphase Flow Simulation of Patient-Specific Total Cavopulmonary Connection Structures Assisted by a Rotationally Symmetric Blood Pump. *Symmetry* **2021**, *13*, 912. <https://doi.org/10.3390/sym13050912>

Academic Editors: Eleuterio F. Toro, Fuyou Liang and Rahmat Ellahi

Received: 19 March 2021

Accepted: 18 May 2021

Published: 20 May 2021

Publisher's Note: MDPI stays neutral with regard to jurisdictional claims in published maps and institutional affiliations.



Copyright: © 2021 by the authors. Licensee MDPI, Basel, Switzerland. This article is an open access article distributed under the terms and conditions of the Creative Commons Attribution (CC BY) license (<https://creativecommons.org/licenses/by/4.0/>).

Abstract: To accurately assess the hemolysis risk of the ventricular assist device, this paper proposed a cell destruction model and the corresponding evaluation parameters based on multiphase flow. The single-phase flow and multiphase flow in two patient-specific total cavopulmonary connection structures assisted by a rotationally symmetric blood pump (pump-TCPC) were simulated. Then, single-phase and multiphase cell destruction models were used to evaluate the hemolysis risk. The results of both cell destruction models indicated that the hemolysis risk in the straight pump-TCPC model was lower than that in the curved pump-TCPC model. However, the average and maximum values of the multiphase flow blood damage index (mBDI) were smaller than those of the single-phase flow blood damage index (BDI), but the average and maximum values of the multiphase flow particle residence time (mPRT) were larger than those of the single-phase flow particle residence time (PRT). This study proved that the multiphase flow method can be used to simulate the mechanical behavior of red blood cells (RBCs) and white blood cells (WBCs) in a complex flow field and the multiphase flow cell destruction model had smaller estimates of the impact shear stress.

Keywords: axial blood pump; computational fluid dynamics; hemolysis risk; multiphase flow; total cavopulmonary connection

1. Introduction

Single ventricular physiology is one of the most severe forms of congenital heart disease. The symmetrical structure of the heart is destroyed, and patients need to be treated immediately after birth. As the final step of three-stage palliative surgery, Fontan surgery directly connects the superior vena cava (SVC) and inferior vena cava (IVC) to the pulmonary artery to form a total cavopulmonary connection (TCPC) physiological structure. After surgery, the essential pumping power for both systemic and pulmonary circulation is provided by a single ventricle, and the burden of that ventricle increases with the patient's age. Approximately 40% of patients will suffer from early heart failure [1], and the survival rate of patients after 5 years is approximately 50% [2].

The cavopulmonary assist devices for Fontan circulation can provide patients with stable and effective biventricular blood flow, which contributes to early surgical repair and the treatment of long-term complications [3]. Among them, the axial blood pump is

a well-developed cavopulmonary assist device [4,5]. Bhavsar et al. designed a magnetic suspension axial blood pump, which was placed in the IVC of TCPC to promote blood flow into the lungs and increase cardiac output [6]. Jagani et al. proposed a symmetrical dual-propeller pump to produce pressure rise in SVC and IVC, and prevent blood from crossing into the opposite vena cava [7].

Generally, axial blood pumps work at high rotating speeds. The RBCs aggregate after being exposed to the high-shear flow field, and the viscosity changes [8]. However, many researchers ignored this phenomenon when assessing the hemolysis risk in blood pumps. They considered the blood as a single-phase Newtonian fluid and used the material properties of the whole blood for simulation, which caused errors in assessing the hemolysis risk [9–11]. A few studies focused on the changes in blood viscosity. Bhavsar et al. [6] studied simulations using different whole blood viscosities and found that high-viscosity blood affected the pressure output and hemolysis risk. Besides, some scholars used non-Newtonian fluid models to characterize changes in blood viscosity due to shear strain rate. Mohammed et al. [12] compared two models for non-Newtonian blood flow to the Newtonian model in the study of the positive displacement left ventricular assist device (LVAD). The results showed that turbulence kinetic energy was generally predicted to be higher in non-Newtonian flow than that observed in Newtonian flow. In a study of axial flow LVAD, Kannojiya et al. used Newtonian fluid and non-Newtonian fluid to simulate blood flow, and found that the differences in flow rate and shear stress were 2.33% and 1.66% respectively [13]. The above studies considered the change of blood viscosity, but still cannot accurately simulate the viscosity change of RBCs. It is a more advanced research taking RBC aggregation into account and calculating the shear rate and viscosity of RBCs when evaluating hemolysis risk. Quemada et al. [14] provided the relationship between viscosity and shear rate of RBCs.

The widely used single-phase flow simulation cannot simulate the mechanical behavior of RBCs. In recent studies, multiphase flow theory has been applied in more fields of hemodynamics [15–18]. Jung et al. [8] used Euler–Euler method to simulate the multiphase flow of blood cells (red blood cells, white blood cells and platelets) and plasma and analyzed the mechanical behavior of blood cells. In the Euler–Euler approach, the different phases of blood are treated as interpenetrating continua and the concept of phasic volume fraction is introduced. These volume fractions are assumed to be continuous functions of space and time and their sum is equal to one [19]. In single-phase flow simulation, RBCs are assumed to be evenly and symmetrically distributed in the blood, and the aggregation of RBCs in high-shear flow field cannot be simulated. However, this asymmetric distribution can be reflected by volume fraction of RBCs in multiphase flow simulation. This study used Euler–Euler method and Quemada model to perform multiphase flow simulation. Furthermore, the single-phase flow cell destruction model does not consider the effect of viscosity on the stress of RBCs. We improved this cell destruction model to obtain a multiphase flow cell destruction model, which considers the RBC viscosity and calculates the hemolysis risk based on the accumulation of shear stress on the RBCs. Simultaneously, we proposed new parameters to assess the hemolysis risk: multiphase flow blood damage index (mBDI) and multiphase flow particle residence time (mPRT).

To confirm the feasibility and superiority of multiphase flow simulation and multiphase flow cell destruction model, we applied the single-phase flow and multiphase flow models to simulate the blood flow in the patient-specific TCPC structures assisted by a blood pump, applied two cell destruction models to assess the hemolysis risk, and compared the evaluation results. The outline of this paper is as follows: in Section 2, we introduced the virtual implantation of axial blood pump, mesh generation of geometric models and CFD settings of cases. Besides, theories of two cell destruction models were illustrated in detail. In Section 3, the hemolysis risk of two pump-TCPC models obtained by single-phase flow and multiphase flow cell destruction model were compared. Further discussion of these results was presented in Section 4. Subsequently, the normalized concentrations of blood cells were shown to verify the feasibility of the multiphase flow

simulation and the choice of turbulence models was discussed. Finally, conclusions were drawn in Section 5.

This article innovatively applied multiphase flow theory to the study of hemolysis in blood pumps. The hemolysis was modeled at the cellular level as well as an advanced cell destruction model was proposed.

2. Materials and Methods

2.1. Acquisition of Patient-Specific TCPC Models and Virtual Implantation of Axial Blood Pump

The axial blood pump designed by our group has been proven to serve as a long-term mechanical assistant with a low risk of blood trauma [20]. This pump consists of the protective housing, inducer, impeller, diffuser and straightener as shown in Figure 1. All parts of the blood pump are designed as rotationally symmetric structure to ensure stable and continuous output.

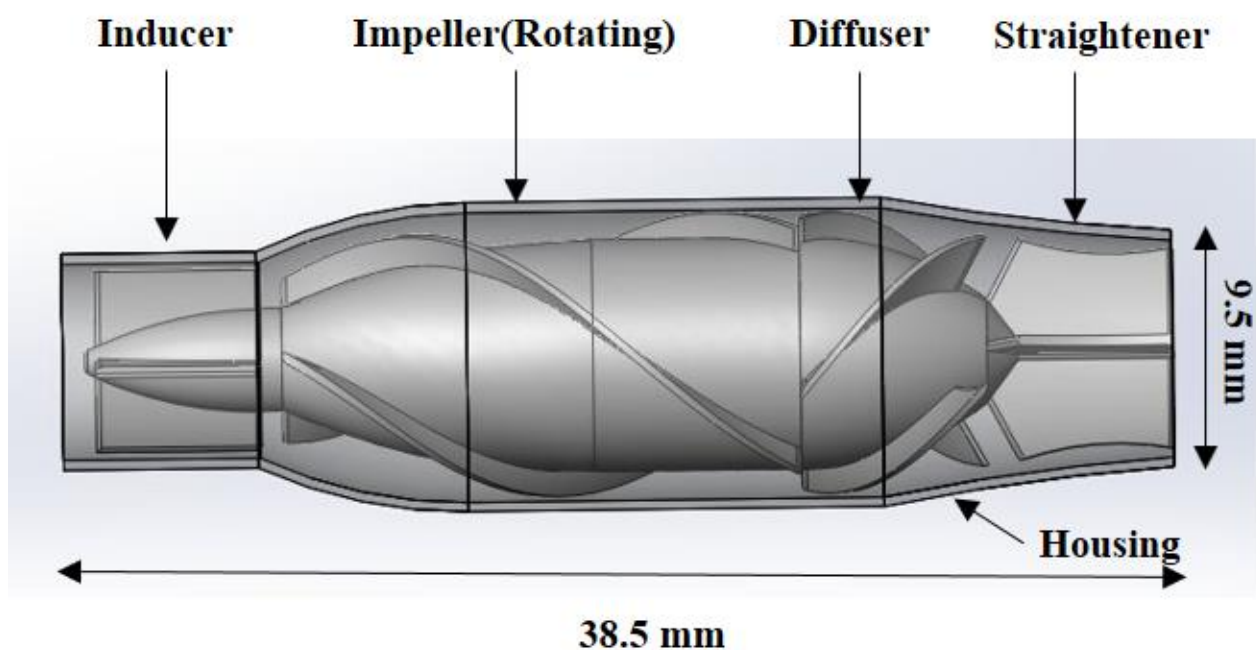


Figure 1. Structure of the axial blood pump.

The straight TCPC model with bilateral SVC was extracted from a 13-year-old female patient, and the curved TCPC model with an extracardiac conduit was extracted from a 14-year-old male patient. First, the Siemens Dual Source CT Scanner (Siemens Healthineers AG, Erlangen, Germany) was used to collect the original DICOM data of two patient-specific TCPC physiological structures. Next, three-dimensional reconstruction of the DICOM data was performed in Mimics 17.0 (Materialise NV Corporation, Gent, Belgium). Then, in Geomagic studio 13.0 (Raindrop Corporation, Ashland, OH, USA), the geometric model was divided into the superior vena cava-pulmonary artery part and inferior vena cava-hepatic vein part according to the implantation position of the axial blood pump. Finally, the two parts and axial blood pump model were assembled in SolidWorks 2015 (SolidWorks Corporation, Concord, MA, USA) to produce the straight and curved pump-TCPC models. Two TCPC models and two pump-TCPC models are shown in Figure 2.

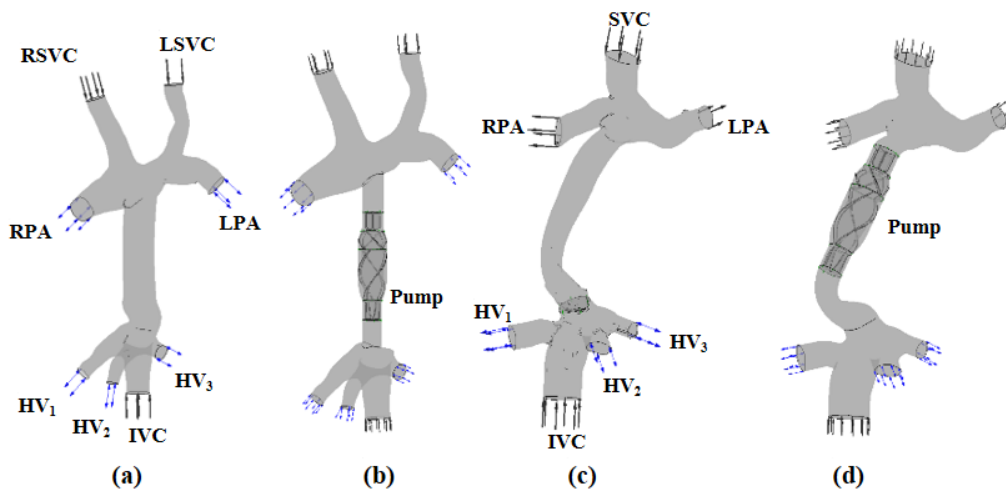


Figure 2. Straight and curved TCPC models of patients and straight and curved pump-TCPC models: (a) straight TCPC model; (b) straight pump-TCPC model; (c) curved TCPC model; (d) curved pump-TCPC model. Abbreviations: LSVC, left superior vena cava; RSVC, right superior vena cava; IVC, inferior vena cava; LPA, left pulmonary artery; RPA, right pulmonary artery; HV1, HV2 and HV3, three hepatic veins.

2.2. Governing Equations

Our previous study discussed in detail the simulation of single-phase flow in the blood pump [20]. Continuity equation in the multiphase flow simulation is shown in Equation (1) [8]:

$$\frac{\partial(\rho_k \varepsilon_k)}{\partial t} + \nabla \cdot (\rho_k \varepsilon_k \vec{v}_k) = 0 \quad (1)$$

where k represents three different phases (plasma, RBCs and WBCs), ρ is density, ε is volume fraction, v is velocity. The volume fraction of three phases satisfies the following equation:

$$\sum_{k=1}^3 \varepsilon_k = 1 \quad (2)$$

The momentum equation in the multiphase flow simulation is as follows [8]:

$$\frac{\partial(\rho_k \varepsilon_k \vec{v}_k)}{\partial t} + \nabla \cdot (\rho_k \varepsilon_k \vec{v}_k \vec{v}_k) = -\varepsilon_k \nabla p + \nabla \cdot \bar{\bar{\tau}}_k + \sum_{\substack{i,k=l,m,n \\ i \neq k}} C_{Dik} (\vec{v}_i - \vec{v}_k) \quad (3)$$

where p is the pressure, C_{Dik} represents the drag coefficient, which indicates the interaction between blood cells and plasma. The Gidaspow model and Schiller–Naumann model are used to simulate the interaction between RBCs and plasma and WBCs and plasma, respectively, as shown in Equations (4) and (5). Re is the Reynolds number. $\bar{\bar{\tau}}$ is the stress tensor of each component, and the stress tensors of plasma and blood cells are defined by Equations (6) and (7). δ is the Kronecker delta, μ is the viscosity, \bar{I} is a unit tensor. κ is the viscosity of whole blood, as shown in Equation (8).

$$C_D = \varepsilon^{-1.65} \max\left(\frac{24}{Re} (1 + 0.15 Re^{0.687}), 0.44\right) \quad (4)$$

$$C_D = \max\left(\frac{24}{Re} (1 + 0.15 Re^{0.687}), 0.44\right) \quad (5)$$

$$\bar{\bar{\tau}} = \varepsilon \mu \left(\nabla \vec{v} + (\nabla \vec{v})^T \right) + \varepsilon \left(\kappa - \frac{2}{3} \mu \right) \nabla \cdot \vec{v} \bar{I} \quad (6)$$

$$\bar{\tau} = -p\delta + \varepsilon\mu \left(\nabla \vec{v} + (\nabla \vec{v})^T \right) + \varepsilon \left(\kappa - \frac{2}{3}\mu \right) \nabla \cdot \vec{v} \bar{I} \quad (7)$$

$$\kappa = \sum_{k=1}^3 \varepsilon_k \mu_k \quad (8)$$

2.3. Mesh Generation

ANSYS-ICEM (ANSYS Incorporated, Canonsburg, PA, USA) was used to generate structured hexahedral elements for the pump model and tetrahedral triangular prism element for the TCPC analyses. A mesh sensitivity analysis was performed to determine the minimum number of cell elements enabling numerical convergence. Six mesh sizes with maximum element size being 1.4 mm, 1.2 mm, 1.0 mm, 0.8 mm, 0.7 mm and 0.6 mm were tested for pump model and seven mesh sizes with maximum element size being 1.4 mm, 1.2 mm, 1.0 mm, 0.8 mm, 0.7 mm, 0.6 mm and 0.5 mm were tested for TCPC model. Energy rise of the blood flow through the pump (Equation (9)) and energy loss through straight TCPC model (Equation (10)) were used as comparison indicators respectively. Results showed that the differences in energy rise (loss) between last two mesh sizes were below 2%. The maximum element sizes of pump and TCPC were set to 0.7 mm and 0.6 mm finally, and element counts of the axial blood pump, straight TCPC and curved TCPC models are listed in Table 1.

$$E_{gain} = E_{outlet} - E_{inlet} = \left(p_{outlet} + \frac{1}{2}\rho v_{outlet}^2 \right) Q_{outlet} - \left(p_{inlet} + \frac{1}{2}\rho v_{inlet}^2 \right) Q_{inlet} \quad (9)$$

$$E_{loss} = E_{inlet} - E_{outlet} = \sum_{inlet} \left(p_{inlet} + \frac{1}{2}\rho v_{inlet}^2 \right) Q_{inlet} - \sum_{outlet} \left(p_{outlet} + \frac{1}{2}\rho v_{outlet}^2 \right) Q_{outlet} \quad (10)$$

where p is the pressure, v is the velocity, ρ is the density and Q is the flow rate.

Table 1. Number of elements of the numerical models.

Models	Element Counts
Axial blood pump model	1383583
Straight pump-TCPC model	2793757
Curved pump-TCPC model	2948813

2.4. Boundary Conditions

The flow rate and pressure waveforms were obtained from clinical measurements of the 14-year-old male patient. All simulations used these waveforms as the boundary conditions. The inlet mass flow rate boundary conditions were specified at the SVC and IVC, as shown in Figure 3a. The blood flow distribution between LSVC and RSVC was set to 40%:60% in the straight pump-TCPC model [21]. To capture all possible reversed flows, three hepatic veins and the left and right pulmonary arteries were given the open boundary condition with the static pressure, as shown in Figure 3b.

We adopted the no-slip boundary condition on the blood vessel walls and outer protective housing of the pump to ensure that the fluid velocity declined to zero as expected. In addition, all walls in the model were modeled as rigid. The impeller domain of the blood pump was set as the clockwise rotation region with a speed of 4000 RPM, while other domains were stationary. The frozen rotor interfaces coupled the impeller domain with other parts through the general grid interface (GGI) method [22].

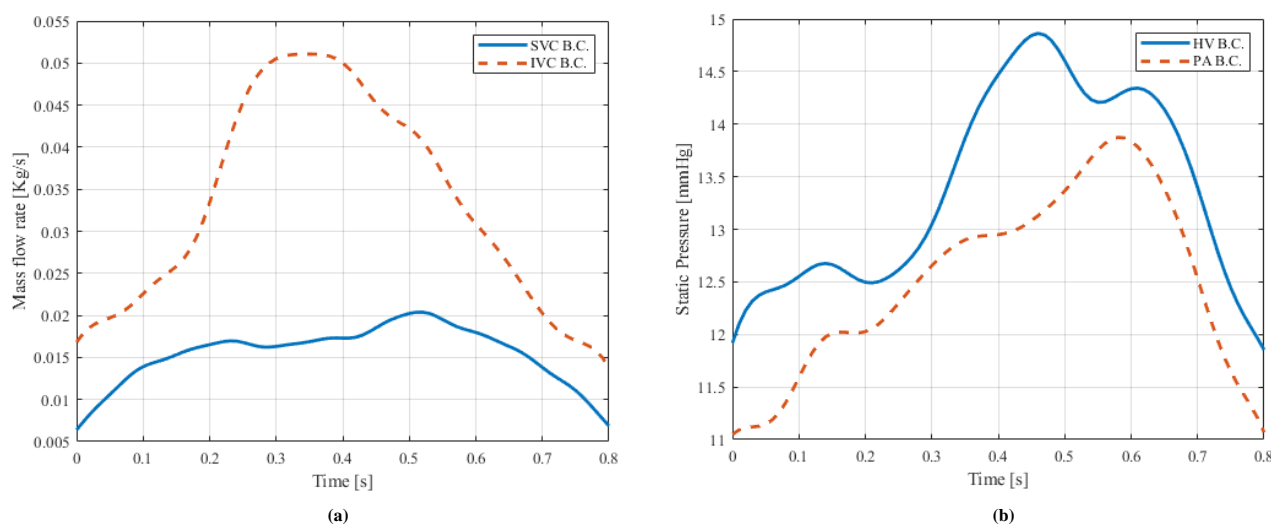


Figure 3. Flow rate profile and pressure profile as the boundary conditions. (a) mass flow rate at SVC (solid line) and IVC (dot line); (b) static pressure at HV (solid line) and PA (dot line). Abbreviations: SVC, superior vena cava; IVC, inferior vena cava; PA, pulmonary artery; HV, hepatic veins.

2.5. Material Properties of the Blood Components

In the single-phase flow simulation, the whole blood was considered as a single-phase Newtonian fluid. In the multiphase flow simulation, blood was modeled as a multiphase mixture composed of plasma, RBCs and WBCs. Plasma was considered as the pure fluid, and RBCs and WBCs were modeled by solid spherical particles with the diameters of 7.2 μm and 11 μm . In addition, the viscosity of RBCs in the multiphase flow simulation was expressed by Quemada model as [17]:

$$\mu_{rbc} = \frac{\mu_p \left(1 - 0.5r_{rbc} \left(k_\infty + \frac{k_0 - k_\infty}{1 + (\dot{\gamma} / \dot{\gamma}_c)^q} \right) \right)^{-2}}{r_{rbc}} - \mu_p r_p \tag{11}$$

where μ_{rbc} is the viscosity of RBCs; r_p and r_{rbc} are the volume fractions of plasma and RBCs; $\dot{\gamma}$ is the shear strain rate of RBCs; k_0 and k_∞ are the intrinsic viscosities for $\dot{\gamma} \rightarrow 0$ and $\dot{\gamma} \rightarrow \infty$; $\dot{\gamma}_c$ is the critical shear strain rate; μ_p is the viscosity of plasma. The values of parameters in Quemada model were obtained from van Weert et al. and listed in Table 2 [23]. The material properties in two simulations are shown in Table 3 [24,25].

Table 2. Parameters of Quemada viscosity model [23].

Parameter	Value
k_∞	1
k_0	$55r_{rbc}^{0.7}e^{-6r_{rbc}} + 1.9$
$\dot{\gamma}_c$	$1.65(r_{rbc} + 0.05)^{-0.3}$
q	0.5

Table 3. Material properties of the blood components [24,25].

	Single-Phase Flow Simulation		Multiphase Flow Simulation	
	Whole Blood	RBCs	WBCs	Plasma
Density (Kg/m ³)	1060	1090	1040	1030
Dynamic viscosity (Pa·s)	0.0035	μ_{rbc}^1	0.00385	0.0011
Specific heat capacity (kJ/kg/K)	3.594	3.22	3.22	3.93
Volume fractions (%)	100	45	0.5	54.5

¹ μ_{rbc} is the viscosity of RBCs calculated by Quemada model.

2.6. Solver Settings

ANSYS-CFX 15.0 (ANSYS Incorporated, Canonsburg, PA, USA) based on finite volume method [26] was utilized to simulate hemodynamics of two pump-TCPC models. Rotation speed of pump was 4000 rpm and Reynolds number reached 11,000 in each simulation. To model turbulent flow conditions, CFD solver with Reynolds averaged Navier Stokes (RANS) method was used to solve the equations for conservation of mass and momentum. We selected standard k- ϵ turbulence model to ensure equation closure due to the reliability of this model demonstrated by several researchers [27,28]. The second order backward Euler scheme [26] was used for temporal discretization, and timestep was set to 0.0005 s. Two cardiac cycles, corresponding to the calculation time of 1.6 s, were simulated to eliminate the initialization effect. The simulation results of the second cardiac cycle were exported for discussion. A convergence criterion of 10^{-4} was applied in this study.

2.7. Single-Phase Flow Cell Destruction Model

Damaged RBCs release hemoglobin into the plasma when hemolysis occurs. Due to the selectivity of the cell membrane, hemoglobin cannot penetrate RBCs. Therefore, the content of hemoglobin in plasma can be used as an evaluation index of cell damage. Previous studies have found that the hemoglobin concentration in plasma is related to the impact shear stress and exposure time of RBCs under the stress. Bludszuweit et al. [29,30] calculated the scalar stress based on the comparative stress theory, as shown in Equation (12):

$$\sigma = \left(\frac{1}{6} \sum (\sigma_{ii} - \sigma_{jj})^2 + \sum \sigma_{ij}^2 \right)^{1/2} \quad (12)$$

where σ is the scalar stress, σ_{ij} represents the component of stress tensor. Giersiepen et al. [31] proposed the exponential relationship among impact shear stress, exposure time and relative change in plasma hemoglobin concentration as shown in Equation (13):

$$dHb/Hb = C \cdot \sigma^\alpha \cdot T^\beta \quad (13)$$

where Hb is the plasma hemoglobin concentration, dHb is the change in plasma hemoglobin concentration due to blood cell damage, σ denotes the scalar stress, T signifies the exposure time and C , α , and β are constants (1.8×10^{-6} , 1.991 and 0.765, respectively) [32].

The degree of destruction of RBCs can be estimated by integrating Equation (13) along streamlines in the blood pump. The dimensionless blood damage index (BDI) is shown in Equation (14):

$$BDI = \int_{inlet}^{outlet} 1.8 \times 10^{-6} \cdot \sigma^{1.991} \cdot dT^{0.765} = \sum_{inlet}^{outlet} 1.8 \times 10^{-6} \cdot \sigma^{1.991} \cdot \Delta T^{0.765} \quad (14)$$

According to the related research of cell destruction in a vane pump [6,33], the blood damage index (BDI) and particle residence time (PRT) could be used to assess the hemolysis risk, and the threshold for cell destruction was set to $BDI = 2\%$ and $PRT = 0.6$ s [34].

2.8. Multiphase Flow Cell Destruction Model

To obtain the multiphase flow cell destruction model, we improved the single-phase flow cell destruction model in two aspects: definition of the scalar stress and relationship between the change in plasma hemoglobin concentration, the scalar stress and exposure time. Blackshear et al. [35] conducted a hemolysis experiment and proposed the relationship between shear stress, exposure time and hemolysis risk, as shown in Equation (15):

$$\tau^2 \cdot T = C_1 \quad (15)$$

where τ is the shear stress, T denotes the exposure time and C_1 signifies a constant of proportionality. Heuser et al. [36] also proposed the relationship among the relative change

in plasma hemoglobin concentration, shear stress and exposure time through hemolysis experiments, as shown in Equation (16):

$$dHb/Hb \propto (\tau^2 \cdot T) \quad (16)$$

Based on Equations (13), (15) and (16), we proposed a new relationship among the change in plasma hemoglobin concentration, scalar shear stress on RBCs, and exposure time in Equation (17):

$$dHb/Hb = C_2 \cdot (\tau_{rbc}^2 \cdot T)^\alpha = C_2 \cdot \tau_{rbc}^{2\alpha} \cdot T^\alpha \quad (17)$$

where α follows the experimental results of Mitamura et al. [32] and is set to 0.765. After a series of simulations, the amplification factor C_2 is set to 1×10^{-6} , so that the blood damage index calculated by Equation (17) is consistent with that calculated by the single-phase flow cell destruction model. Therefore, the risk threshold of the new cell destruction model can be set to 2%. The dimensionless multiphase flow blood damage index (mBDI) is expressed by Equation (18):

$$mBDI = \int_{inlet}^{outlet} 1 \times 10^{-6} \cdot \tau_{rbc}^{1.53} \cdot dT^{0.765} = \sum_{inlet}^{outlet} 1 \times 10^{-6} \cdot \mu_{rbc}^{1.53} \cdot \dot{\gamma}_{rbc}^{1.53} \cdot \Delta T^{0.765} \quad (18)$$

where μ_{rbc} is the viscosity of RBCs calculated by Quemada model, T is the exposure time, and $\dot{\gamma}_{rbc}$ is the scalar shear strain rate of RBCs, expressed by Equation (19) [26]:

$$\dot{\gamma}_{rbc} = \left[2 \left\{ \left(\frac{\partial U_x}{\partial x} \right)^2 + \left(\frac{\partial U_y}{\partial y} \right)^2 + \left(\frac{\partial U_z}{\partial z} \right)^2 \right\} + \left(\frac{\partial U_x}{\partial y} + \frac{\partial U_y}{\partial x} \right)^2 + \left(\frac{\partial U_x}{\partial z} + \frac{\partial U_z}{\partial x} \right)^2 + \left(\frac{\partial U_y}{\partial z} + \frac{\partial U_z}{\partial y} \right)^2 \right]^{1/2} \quad (19)$$

where U_x , U_y and U_z represent the velocity components in each coordinate direction.

Corresponding to PRT, in the multiphase flow cell destruction model, we proposed the multiphase flow particle residence time (mPRT) to represent the time that a particle travels from the inlet to the outlet. Both mPRT and PRT represent the same physical quantities, so the threshold of mPRT is set to 0.6 s, which is equal to that of PRT.

3. Results

Two cell destruction models were applied to evaluate the hemolysis risk in the entire pump-TCPC model. At 0.2 s, 0.35 s, 0.6 s, and 0.8 s of the second cardiac cycle (which correspond to the maximum acceleration instant, maximum speed instant, maximum deceleration instant, and minimum speed instant of the IVC boundary condition), 300 particles were released at the IVC inlet of the straight and curved pump-TCPC models. Then, the BDI, PRT, mBDI and mPRT of each particle were calculated.

The distributions of particle BDI in the straight and curved pump-TCPC models are shown in Figure 4, and the average and maximum values of BDI and PRT of 300 particles are shown in Table 4. All average values of BDI are smaller than 2%, and most average values of PRT are smaller than 0.6. Only when at 0.8 s, is the average PRT in the curved model larger than 0.6. Hence, the hemolysis risk is low in both straight model and curved model when the axial pump is rotating.

The hemolysis risks in two pump-TCPC models were compared based on the following criteria: smaller BDI and PRT values represent lower hemolysis risk and higher clinical value. First, for the average BDI parameter, the straight model is superior to the curved model at the first three moments, while the curved model is superior at the last moment. Next, for the maximum BDI parameter, the straight model is inferior at all moments, but Figure 4 shows that this phenomenon is caused by a very small number of particles. Third, for the average PRT parameter, the straight model is superior at all moments. Fourth, for the maximum PRT parameter, the curved model is superior at 0.2 s and 0.35 s, while the straight model is superior at 0.6 s and 0.8 s. Based on the comprehensive analysis of four

parameters, we can conclude that the hemolysis risk is lower in the straight model under single-phase flow simulation.

The distributions of particle mBDI in the straight and curved pump-TCPC models are shown in Figure 5. The average and maximum values of the mBDI and mPRT are shown in Table 5. All average values of mPRT are greater than 0.6, and all average and maximum values of mBDI are smaller than 2%. Although the average residence time of particles exceeds the threshold, RBCs are less damaged outside the blood pump. Therefore, the hemolysis risks are low in both straight model and curved model under the multiphase simulation.

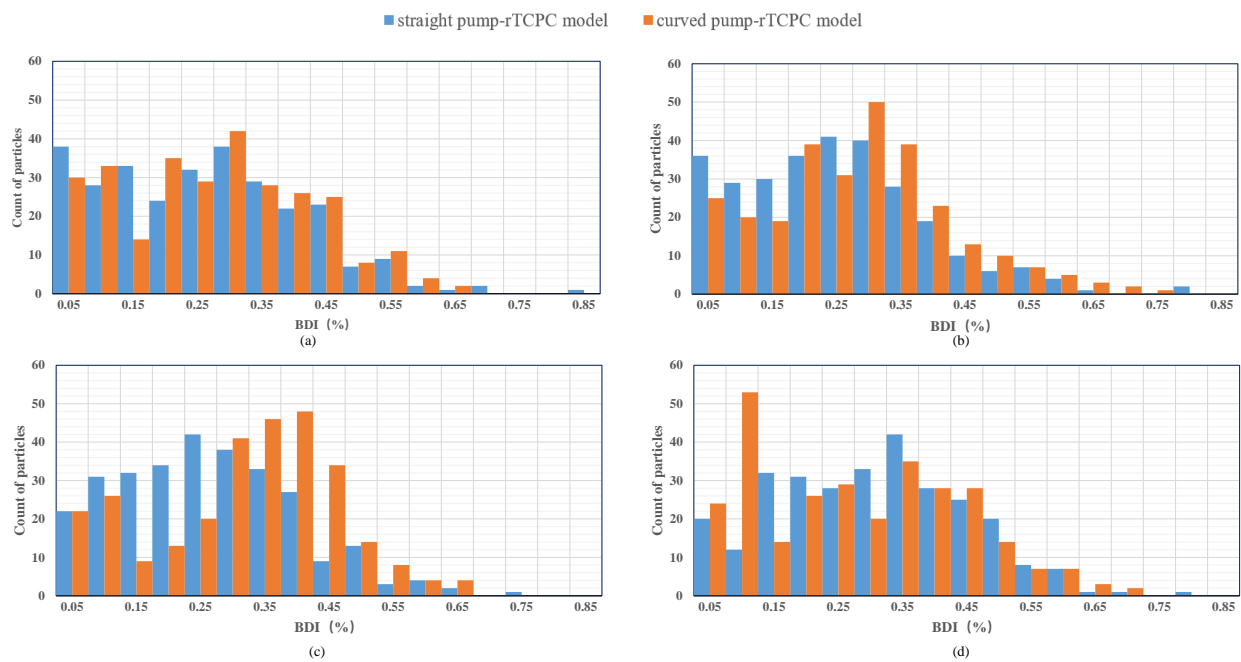


Figure 4. Distributions of particle BDI in the straight and curved pump-TCPC models at different moments (a–d: distributions of particle BDI at 0.2 s, 0.35 s, 0.6 s, and 0.8 s).

Table 4. Assessment parameters of hemolysis risk in straight and curved pump-TCPC models under the single-phase flow simulation.

Time	Average PRT (s)		Maximum PRT (s)		Average BDI (100%)		Maximum BDI (100%)	
	Straight	Curved	Straight	Curved	Straight	Curved	Straight	Curved
0.2 s	0.41	0.53	1.64	1.07	0.24	0.25	0.82	0.64
0.35 s	0.34	0.42	2.20	1.25	0.22	0.26	0.77	0.71
0.6 s	0.38	0.58	1.07	1.61	0.24	0.29	0.71	0.65
0.8 s	0.52	0.77	1.24	1.45	0.28	0.25	0.76	0.67

Table 5. Assessment parameters for the hemolysis risk in straight and curved pump-TCPC models under multiphase flow simulation.

Time	Average mPRT (s)		Maximum mPRT (s)		Average mBDI (100%)		Maximum mBDI (100%)	
	Straight	Curved	Straight	Curved	Straight	Curved	Straight	Curved
0.2 s	0.74	1.04	2.63	2.68	0.21	0.23	0.54	0.61
0.35 s	0.75	0.80	4.04	1.78	0.21	0.23	0.53	0.50
0.6 s	0.81	1.02	5.23	2.39	0.22	0.25	0.48	0.64
0.8 s	1.01	1.41	4.15	3.94	0.23	0.23	0.48	0.57

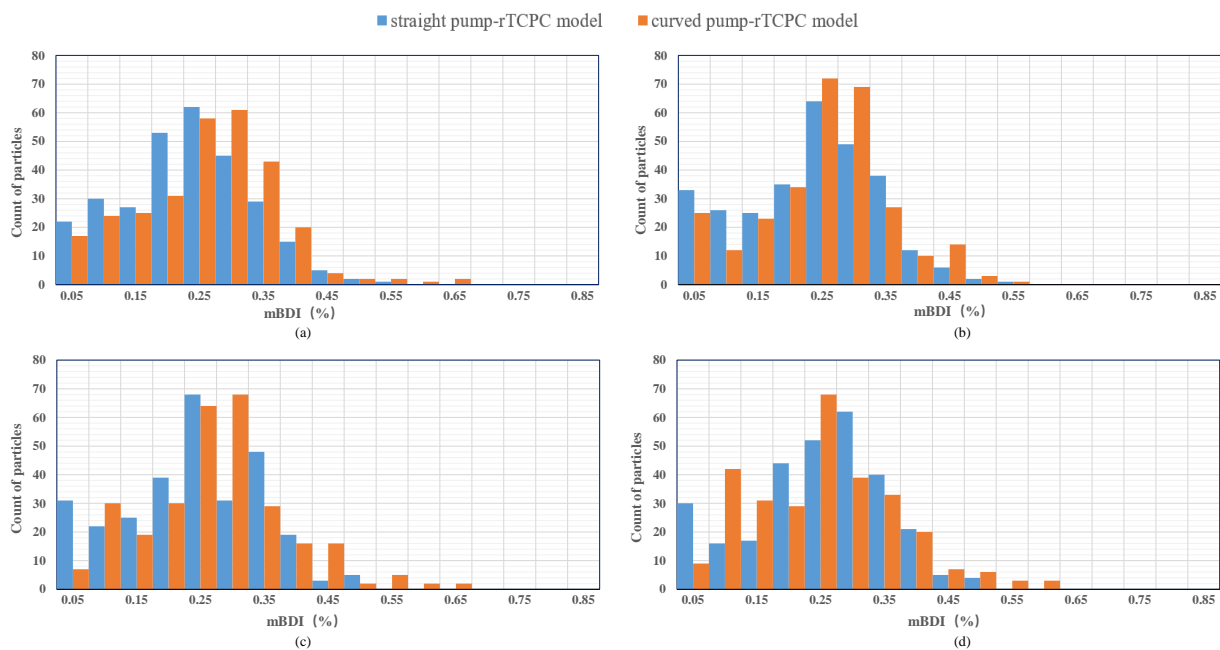


Figure 5. Distribution of particle mBDI in the straight and curved pump-TCPC models at different moments (a–d: distributions of particle mBDI at 0.2 s, 0.35 s, 0.6 s, and 0.8 s).

Similarly, we compared the hemolysis risk in straight and curved models. First, for the average and maximum mBDI parameters, the straight model is superior to the curved model in most cases. There are only two counter examples. At 0.8 s, the average mBDI values in the straight and curved models are identical. At 0.35 s, the straight model is inferior to the curved model on the maximum mBDI parameter, and Figure 5b shows that this phenomenon is caused by a very small number of particles. Second, for the average mPRT parameter, the straight model is superior to the curved model, but for the maximum mPRT parameter, the straight model is inferior to the curved model, which reflects the complexity of the flow field in the multiphase flow simulation. Through the analysis of the four indicators, we can also conclude that the hemolysis risk in the straight model is smaller under the multiphase flow simulation.

Moreover, Figures 4 and 5 show that the distributions of BDI in the straight and curved models are concentrated at approximately 0.3%, while the distributions of mBDI are concentrated at approximately 0.25%.

4. Discussion

Comparisons between mBDI and BDI and between mPRT and PRT are shown in Tables 6 and 7. We know that the assessment of hemolysis risk changes after considering the viscosity change of RBCs. As shown in Table 6, all average mBDI and maximum mBDI values are smaller than the corresponding average BDI and maximum BDI, and the maximum relative change rates of the average and maximum values are 17.8% and 36.8%. Table 7 shows that all average mPRT and maximum mPRT values are larger than the corresponding average PRT and maximum PRT, and the maximum relative change rates of the average and maximum values are 120.6% and 388.8%. In other words, the residence time of cells are longer in the multiphase flow simulation, but fewer cells are damaged. The blood damage index was calculated by integrating the impact shear stress and exposure time along the streamlines. Therefore, the estimates of impact shear stress are smaller in multiphase simulations.

Table 6. Comparison between BDI and mBDI.

Time	Straight Pump-TCPC Model						Curved Pump-TCPC Model					
	Average Value (%)		Rcr* (%)	Maximum Value (%)		Rcr* (%)	Average Value (%)		Rcr* (%)	Maximum Value (%)		Rcr* (%)
	BDI	mBDI		BDI	mBDI		BDI	mBDI		BDI	mBDI	
0.2 s	0.24	0.21	12.5	0.82	0.54	34.1	0.25	0.23	8	0.64	0.61	4.7
0.35 s	0.22	0.21	4.5	0.77	0.53	31.2	0.26	0.23	11.5	0.71	0.50	29.6
0.6 s	0.24	0.22	8.3	0.71	0.48	32.4	0.29	0.25	13.8	0.65	0.64	1.5
0.8 s	0.28	0.23	17.8	0.76	0.48	36.8	0.25	0.23	8	0.67	0.57	14.9

rcr* is the relative change rate of mBDI to BDI, which is calculated as follows: $\left| \frac{mBDI - BDI}{BDI} \right| * 100\%$.

Table 7. Comparison between PRT and mPRT.

Time	Straight Pump-TCPC Model						Curved Pump-TCPC Model					
	Average Value (%)		Rcr# (%)	Maximum Value (%)		Rcr# (%)	Average Value (%)		Rcr# (%)	Maximum Value (%)		Rcr# (%)
	PRT	mPRT		PRT	mPRT		PRT	mPRT		PRT	mPRT	
0.2 s	0.41	0.74	80.5	1.64	2.63	60.4	0.53	1.04	96.2	1.07	2.68	150.5
0.35 s	0.34	0.75	120.6	2.20	4.04	83.6	0.42	0.80	90.5	1.25	1.78	42.4
0.6 s	0.38	0.81	113.2	1.07	5.23	388.8	0.58	1.02	75.9	1.61	2.39	48.5
0.8 s	0.52	1.01	94.2	1.24	4.15	234.7	0.77	1.41	83.1	1.45	3.94	171.7

rcr# is the relative change rate of mPRT to PRT, which is calculated as follows: $\left| \frac{mPRT - PRT}{PRT} \right| * 100\%$.

To verify the feasibility of the multiphase flow simulation, we performed a steady-state simulation of the axial blood pump. The inlet flow rate is 1.8 L/min, the outlet pressure is 40 mmHg, and the rotation speed is 4000 RPM. The normalized concentrations of blood cells are defined as the local concentration divided by their inlet concentration (45% for RBCs and 0.5% for WBCs).

WBCs have a higher aggregation degree than RBCs. The ranges of normalized concentrations of RBCs on the wall of the blades and inner wall of the housing are 99.46–100.3% and 99.98–100.14%. The ranges of normalized concentrations of WBCs are 86.9–105.2% and 97.3–100.7%. In Figure 6a,c, blood cells are mainly concentrated on the leading edge of blades of the inducer, diffuser and straightener. The areas with low blood cells concentration symmetrically distribute on the surface and trailing edge of the inducer blades, which is related to the flow separation. In addition, the areas with low WBC concentration are larger than that with low RBC concentration. These differences in normalized concentration of RBCs and WBCs are consistent with the results in study of Ou et al. [17]. As shown in Figure 6b,d, the areas with high RBC concentration symmetrically distribute near the impeller blades, but the concentration of WBCs is low in these area. When the impeller is rotating, RBCs migrate towards the inner wall of the housing under centrifugal force, while WBCs remain on the surface of the impeller. These results further prove the feasibility of the multiphase flow simulation.

The simulation of turbulence has always been a challenge in study of blood pump. The accuracy of turbulence solution has a great influence on the distribution of pressure and velocity, and then affects the evaluation of pressure rise and hemolysis risk. Large eddy simulations can handle the anisotropic turbulent flow features present in blood flow [37]. However, it will cost extensive resources to apply large eddy simulation to the study of blood pump. RANS-based turbulence models are frequently used in the engineering applications because they are more economical in terms of computing resources and time efficiency. The standard k-ε model is one of the most commonly used models, and its reliability has been confirmed by many researchers. For example, the standard k-ε model turbulence model has been used for several years in designing axial blood pump prototypes in the research of Throckmorton et al. [2,38–40]. In the research of PVAD3,

Throckmorton et al. compared the experimental data with the simulation results obtained from multiple turbulence models (standard k- ϵ , k- ω , and shear stress transport) found that the difference between the results of the standard k- ϵ model and the experimental data is the smallest [27]. This paper also proposed the equation for estimating global Re in the study of axial blood pump:

$$Re = \frac{\rho\omega D^2}{\mu} \quad (20)$$

where ρ and μ represent the fluid density and viscosity, ω is the angular speed of the impeller, D signifies the impeller diameter.

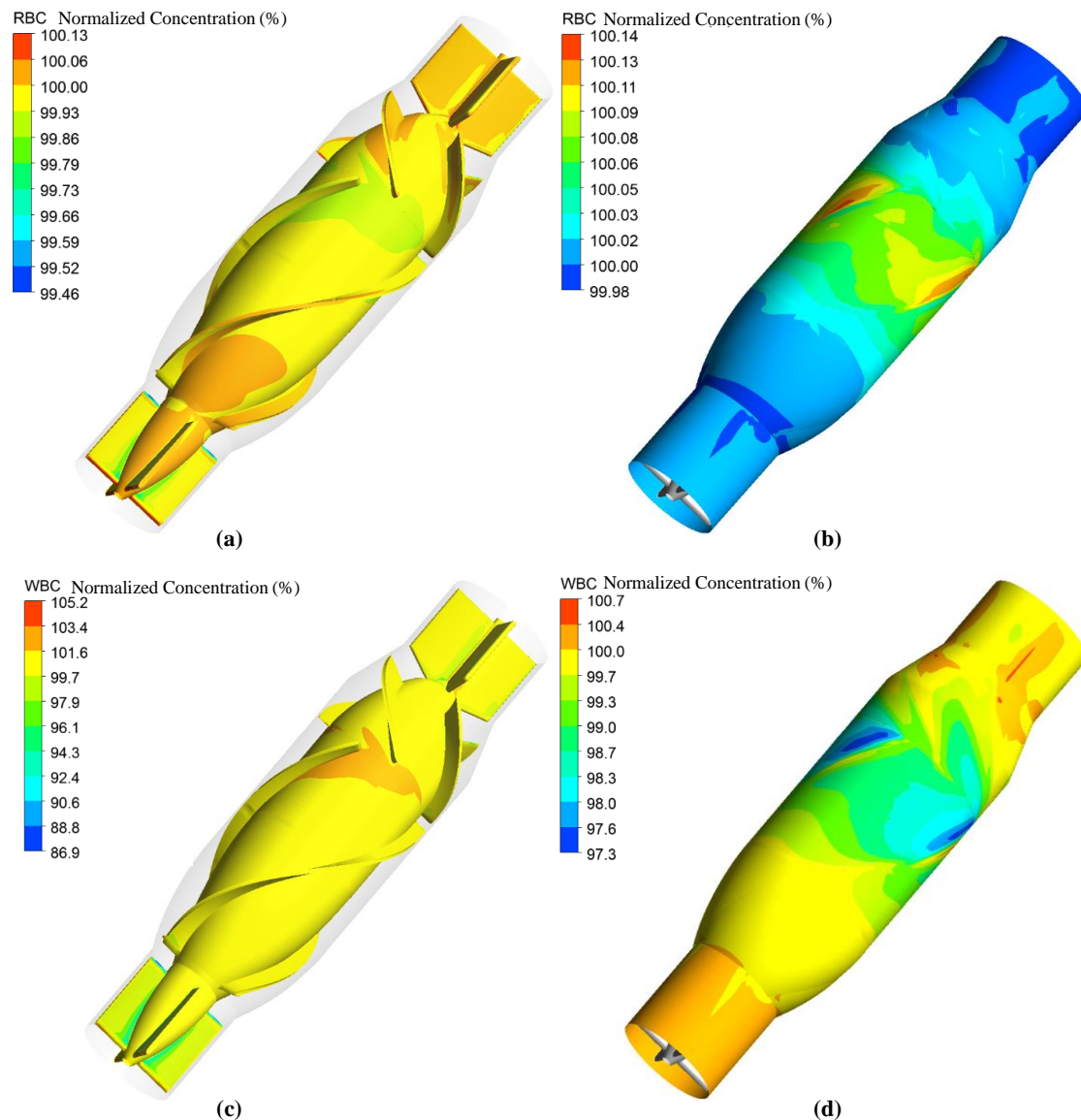


Figure 6. Normalized concentrations of blood cells on the wall (a,c: normalized concentrations of RBCs and WBCs on the wall of the blades; b,d: normalized concentrations of RBCs and WBCs on the inner wall of the housing).

According to the above equation, it can be calculated that the global Re in our research is about 11,000, which is similar to the global Re in the research of PVAD3(10^4) [40]. Therefore, it is reasonable to use the standard k- ϵ model in our research. Besides, Apel et al. used the standard k- ϵ model in the CFD study on microaxial blood pump, and used particle-tracking velocimetry (PTV) for quantitative investigation. The results showed that the H-Q curves, exit angles, and swirl in the inlet region predicted by CFD are in good agreement

with the measured results [28]. The large eddy simulation can show finer turbulence characteristics, however, it will cost a lot to apply the large eddy simulation to the research of blood pumps. Drešar et al. used an advanced scale adaptive simulation (SAS-SST) turbulence model and standard SST- $k\omega$ model to conduct the numerical simulation of HeartAssist5 blood pump, and compared simulation results with experimental results [41]. The computation time of two turbulence model was comparable, but smaller and finer turbulent flow characteristics can be observed in results of SAS-SST model. Next, we will compare the differences in evaluating the hemolysis risk using different turbulence models.

Hemolysis experiments were not conducted in this paper, so there is no comparison between experimental data and evaluation results from two cell destruction models. In addition, hemoglobin will be released into the plasma after RBCs have been damaged, which may cause changes in plasma viscosity. This physiological phenomenon is not reflected in the multiphase flow cell destruction model in this paper. Next, we plan to establish a physical model of the TCPC structure of the patient, manufacture the axial blood pump, and perform the hemolysis experiment. After obtaining experiment results, we will compare them with the simulation results to further prove the feasibility and superiority of the multiphase flow simulation and multiphase flow cell destruction model.

5. Conclusions

To assess the hemolysis risk more accurately, this paper proposed an advanced multiphase flow cell destruction model, which evaluated the hemolysis risk based on stress on red blood cells. Single-phase flow and multiphase flow simulations were performed in the straight and curved pump-TCPC models, respectively. It can be concluded that hemolysis risk is lower in the straight pump-TCPC model using both cell destruction models, but the estimation of the impact shear stress in the multiphase flow cell destruction model are smaller. The primary reason for hemolysis is the excessive shear which damages the RBCs and leads to release of hemoglobin. The multiphase flow cell destruction model can better reflect the mechanism of hemolysis. Future studies will focus on hemolysis experiments, which is an essential part to prove the reliability of multiphase flow cell destruction model.

Author Contributions: Conceptualization, X.L., B.J. and S.W.; data curation, B.S., H.Z. and B.J.; Formal analysis, T.C. and X.L.; funding acquisition, S.W.; investigation, T.C., X.L. and B.S.; methodology, T.C., X.L. and Y.F.; project administration, B.J. and S.W.; resources, B.S., H.Z. and B.J.; software, T.C., X.L. and Y.F.; supervision, B.J. and S.W.; validation, T.C. and X.L.; visualization, T.C. and X.L.; writing—original draft, T.C.; writing—review and editing, T.C., X.L. and S.W. All authors have read and agreed to the published version of the manuscript.

Funding: This research was funded by National Natural Science Foundation of China, Grant Number 11872152, 32071310.

Institutional Review Board Statement: Ethical review and approval were waived for this study. All data used in this study did not involve the privacy of patients. This article had no influence on the diagnosis and therapy of patients.

Informed Consent Statement: Informed consent was obtained from all subjects involved in the study.

Data Availability Statement: No new data were created or analyzed in this study. Data sharing is not applicable to this article.

Conflicts of Interest: The authors declare no conflict of interest.

References

1. Throckmorton, A.L.; Chopski, S.G. Pediatric circulatory support: Current strategies and future directions. Biventricular and univentricular mechanical assistance. *ASAIO J.* **2008**, *54*, 491–497. [[CrossRef](#)] [[PubMed](#)]
2. Throckmorton, A.L.; Untaroiu, A. CFD analysis of a Mag-Lev ventricular assist device for infants and children: Fourth generation design. *ASAIO J.* **2008**, *54*, 423–431. [[CrossRef](#)] [[PubMed](#)]
3. Yuan, H.Y.; Chen, J.M.; Zhuang, J. Progress of Cavopulmonary Assisting Device for Fontan Circulation. *Chin. J. Clin. Thorac. Cardiovasc. Surg.* **2016**, *23*, 728–731.

4. Rodefeld, M.D.; Boyd, J.H.; Myers, C.D.; LaLone, B.J.; Bezruczko, A.J.; Potter, A.W.; Brown, J.W. Cavopulmonary assist: Circulatory support for the univentricular fontan circulation. *Ann. Thorac. Surg.* **2003**, *76*, 1911–1916. [CrossRef]
5. Jarvik, R. Jarvik 2000 Pump Technology and Miniaturization. *Heart Fail. Clin.* **2014**, *10*, S27–S38. [CrossRef]
6. Bhavsar, S.S.; Moskowitz, W.B.; Throckmorton, A.L. Interaction of an idealized cavopulmonary circulation with mechanical circulatory assist using an intravascular rotary blood pump. *Artif. Organs* **2010**, *34*, 816–827. [CrossRef] [PubMed]
7. Jagani, J.N.; Untaroiu, A.; Kalaria, A.D. Dual-Propeller cavopulmonary pump for assisting patients with hypoplastic right ventricle. *ASAIO J.* **2019**, *65*, 888–897. [CrossRef]
8. Jung, J.; Hassanein, A.; Lyczkowski, R.W. Hemodynamic computation using multiphase flow dynamics in a right coronary artery. *Ann. Biomed. Eng.* **2006**, *34*, 393–407. [CrossRef]
9. Fraser, K.H.; Zhang, T.; Taskin, M.E.; Griffith, B.P.; Wu, Z.J. A quantitative comparison of mechanical blood damage parameters in rotary ventricular assist devices: Shear stress, exposure time and hemolysis index. *J. Biomech. Eng.* **2012**, *134*, 1–11. [CrossRef]
10. Yano, T.; Sekine, K.; Mitoh, A.; Mitamura, Y.; Okamoto, E.; Kim, D.-W.; Nishimura, I.; Murabayashi, S.; Yozu, R. An estimation method of hemolysis within an axial flow blood pump by computational fluid dynamics analysis. *Artif. Organs* **2003**, *27*, 920–925. [CrossRef]
11. Xia, D.D.; Zhao, C.Z.; Zhang, X.W.; Bai, J. Computational fluid dynamics modeling and hemolysis analysis of axial blood pumps with various impeller structures. *Prog. Nat. Sci. Mater. Int.* **2006**, *16*, 993–997.
12. Al-Azawy, M.G.; Turan, A.; Revell, A. Investigating the impact of non-Newtonian blood models within a heart pump. *Int. J. Numer. Methods Biomed. Eng.* **2017**, *33*, 1–18. [CrossRef]
13. Kannojiya, V.; Das, A.K.; Das, P.K. Proposal of hemodynamically improved design of an axial flow blood pump for LVAD. *Med Biol. Eng. Comput.* **2019**, *58*, 401–418. [CrossRef] [PubMed]
14. Quemada, D. Rheology of concentrated disperse systems II. A model for non-newtonian shear viscosity in steady flows. *Rheol. Acta* **1978**, *17*, 632–642. [CrossRef]
15. Brennen, C.E. Fundamentals of Multiphase Flow. Available online: https://books.google.com/books?hl=zhCN&lr=&id=F7hEfx2GUPYC&oi=fnd&pg=PR13&dq=Fundamentals+of+multiphase+flow&ots=EUakyaqUCL&sig=8JuXfCsnNEo6mKcET_edQmOUuRM#v=onepage&q=Fundamentals%20of%20multiphase%20flow&f=false (accessed on 12 March 2021).
16. Melka, B.; Gracka, M.; Adamczyk, W.; Rojczyk, M.; Golda, A.; Nowak, A.J.; Białecki, R.A.; Ostrowski, Z. Multiphase simulation of blood flow within main thoracic arteries of 8-year-old child with coarctation of the aorta. *Heat Mass Transf.* **2018**, *54*, 2405–2413. [CrossRef]
17. Ou, C.; Huang, W.; Yuen, M.M.-F.; Qian, Y. Hemodynamic modeling of leukocyte and erythrocyte transport and interactions in intracranial aneurysms by a multiphase approach. *J. Biomech.* **2016**, *49*, 3476–3484. [CrossRef] [PubMed]
18. Yilmaz, F.; Kutlar, A.I.; Gundogdu, M.Y. Analysis of drag effects on pulsatile blood flow in a right coronary artery by using Eulerian multiphase model. *Korea-Aust. Rheol. J.* **2011**, *23*, 89–103. [CrossRef]
19. ANSYS. *ANSYS Fluent Theory Guide 2020 R2*; Ansys, Inc.: Canonsburg, PA, USA, 2020.
20. Liu, X.; Cai, Y.; Jia, B.; Wang, S.; Ding, G. Numerical analyses of idealized total cavopulmonary connection physiologies with single and bilateral superior vena cava assisted by an axial blood pump. *Comput. Model. Eng. Sci.* **2018**, *116*, 215–228. [CrossRef]
21. Downs, E.A.; Moskowitz, W.B.; Throckmorton, A.L. Steady flow analysis of mechanical cavopulmonary assistance in MRI-derived patient-specific Fontan configurations. *Artif. Organs* **2012**, *36*, 972–980. [CrossRef] [PubMed]
22. Riemer, R.K.; Amir, G.; Reichenbach, S.H.; Reinhartz, O. Mechanical support of total cavopulmonary connection with an axial flow pump. *J. Thorac. Cardiovasc. Surg.* **2005**, *130*, 351–354. [CrossRef]
23. Van Weert, K. Numerical and Experimental Analysis of Shear-Induced Migration in Suspension Flow. Available online: <https://pure.tue.nl/ws/portalfiles/portal/46908122/633360-1.pdf> (accessed on 12 March 2021).
24. Blake, A.S.; Petley, G.W.; Deakin, C.D. Effects of changes in packed cell volume on the specific heat capacity of blood: Implications for studies measuring heat exchange in extracorporeal circuits. *Br. J. Anaesth. BJA* **2000**, *84*, 28–32. [CrossRef] [PubMed]
25. Bräuer, A. Perioperative Temperature Management. Available online: <https://www.uptodate.com/contents/perioperative-temperature-management> (accessed on 12 March 2021).
26. ANSYS CFX-Solver Theory Guide. Available online: http://download.hangtuah.ac.id/ansys/ansys-2020/Docs/Ansys.Products.PDF.Docs.2020R1/v201/ANSYS_CFX-Solver_Theory_Guide.pdf (accessed on 12 March 2021).
27. Throckmorton, A.L.; Untaroiu, A.; Allaire, P.E.; Wood, H.G.; Lim, D.S.; McCulloch, M.A.; Olsen, D.B. Numerical design and experimental hydraulic testing of an axial flow ventricular assist device for infants and children. *ASAIO J.* **2007**, *53*, 754–761. [CrossRef]
28. Apel, J.; Neudel, F.; Reul, H. Computational fluid dynamics and experimental validation of a microaxial blood pump. *ASAIO J.* **2001**, *47*, 552–558. [CrossRef] [PubMed]
29. Bludszuweit, C. Three-dimensional numerical prediction of stress loading of blood particles in a centrifugal pump. *Artif. Organs* **1995**, *19*, 590–596. [CrossRef]
30. Bludszuweit, C. Model for a general mechanical blood damage prediction. *Artif. Organs* **1995**, *19*, 583–589. [CrossRef] [PubMed]
31. Giersiepen, M.; Wurzinger, L.J.; Opitz, R.; Reul, H. Estimation of shear stress-related blood damage in heart valve prostheses—in vitro comparison of 25 aortic valves. *Int. J. Artif. Organs* **1990**, *13*, 300–306. [CrossRef]
32. Mitamura, Y.; Nakamura, H.; Sekine, K.; Kim, D.W.; Ryohei, Y.; Kawada, S.; Kawada, S.; Okamoto, E. Prediction of hemolysis in rotary blood pumps with computational fluid dynamics analysis. *J. Congest. Heart Fail. Circ. Support* **2000**, *1*, 331–336.

33. Song, X.; Throckmorton, A.L.; Wood, H.G.; Antaki, J.F.; Olsen, D.B. Quantitative evaluation of blood damage in a centrifugal VAD by computational fluid dynamics. *J. Fluids Eng.* **2004**, *126*, 410–418. [[CrossRef](#)]
34. Throckmorton, A.L.; Lopez-Isaza, S.; Moskowitz, W. Dual-Pump support in the inferior and superior vena cavae of a Patient-Specific fontan physiology. *Artif. Organs* **2013**, *37*, 513–522. [[CrossRef](#)]
35. Blackshear, P.L.; Dormen, F.D.; Steinbach, J.H. Some mechanical effects that influence hemolysis. *ASAIO Trans.* **1965**, *11*, 112–117. [[CrossRef](#)]
36. Heuser, G.; Opitz, R. A Couette viscometer for short time shearing of blood. *Biorheology* **1980**, *17*, 17–24. [[CrossRef](#)]
37. Andersson, M.; Karlsson, M. Characterization of anisotropic turbulence behavior in pulsatile blood flow. *Biomech. Model. Mechanobiol.* **2021**, *20*, 491–506. [[CrossRef](#)] [[PubMed](#)]
38. Throckmorton, A.L.; Untaroiu, A.; Allaire, P.E.; Wood, H.G.; Matherne, G.P.; Lim, D.S.; Peeler, B.B.; Olsen, D.B. Computational analysis of an axial flow pediatric ventricular assist device. *Artif. Organs* **2004**, *28*, 881–891. [[PubMed](#)]
39. Untaroiu, A.; Wood, H.G.; Allaire, P.E.; Throckmorton, A.L.; Day, S.; Patel, S.M.; Ellman, P.; Tribble, C.; Olsen, D.B. Computational design and experimental testing of a novel axial flow LVAD. *ASAIO J.* **2005**, *51*, 702–710. [[CrossRef](#)]
40. Throckmorton, A.L.; Untaroiu, A.; Lim, D.S.; Wood, H.G.; Allaire, P.E. Fluid force predictions and experimental measurements for a magnetically levitated pediatric ventricular assist device. *Artif. Organs* **2007**, *31*, 359–368. [[CrossRef](#)] [[PubMed](#)]
41. Drešar, P.; Rutten, M.C.M.; Gregorič, I.D.; Duhovnik, J. A numerical simulation of HeartAssist5 blood pump using an advanced turbulence model. *ASAIO J.* **2018**, *64*, 673–679. [[CrossRef](#)] [[PubMed](#)]